HHS Public Access

Author manuscript

Nat Struct Mol Biol. Author manuscript; available in PMC 2019 September 04.

Published in final edited form as:

Nat Struct Mol Biol. 2019 March ; 26(3): 220–226. doi:10.1038/s41594-019-0193-2.

A gel phase promotes condensation of liquid P granules in *C. elegans* embryos

Andrea Putnam[1], **Madeline Cassani**[1], **Jarrett Smith**[1,2], **Geraldine Seydoux**[1]

[1.]Department of Molecular Biology and Genetics, Howard Hughes Medical Institute, Johns Hopkins University, School of Medicine, Baltimore, MD, USA

[2.]Present address: Jarrett Smith: Whitehead Institute, Massachussets Institute of Technology, Boston, MA, USA.

Abstract

RNA granules are sub-cellular compartments proposed to form by liquid-liquid phase separation (LLPS), a thermodynamic process that partitions molecules between dilute and condensed liquid phases. The mechanisms that localize liquid phases in cells, however, are not fully understood. P granules are RNA granules that form in the posterior of *C. elegans* embryos. Theoretical studies have suggested that spontaneous LLPS of the RNA-binding protein PGL-3 with RNA drives P granule assembly. We find that the PGL-3 phase is intrinsically labile and requires a second phase for stabilization in embryos. The second phase is formed by gel-like assemblies of the disordered protein MEG-3 that associate with liquid PGL-3 droplets in the embryo posterior. Co-assembly of gel and liquid phases confers local stability and long-range dynamics, both of which contribute to localized P granule assembly. Our findings suggest that condensation of RNA granules can be regulated spatially by gel-like polymers that stimulate LLPS locally in the cytoplasm.

Liquid-liquid phase separation (LLPS) is a spontaneous de-mixing process where molecules partition between condensed and dilute liquid phases [1,2]. LLPS has been proposed to underlie the formation of RNA granules in cells, and several RNA-binding proteins have been found to undergo LLPS *in vitro* [3]. Some LLPS condensates assembled *in vitro* mature over time into non-dynamic, gel-like condensates [4–7]. Solidification of liquid phases in RNA granules has been linked to pathological states, as in certain neurodegenerative diseases where RNA granule components become trapped in non-dynamic aggregates [2,8]. Solid cores have also been observed in stress granules, but whether they are by-products of LLPS or essential structures that support granule assembly is not yet known [9,10]. Here, we have investigated a possible role for non-dynamic condensates in the formation of P granules, dynamic RNA granules that form under normal conditions in the germline of *C. elegans*.

Corresponding Author Statement: Correspondence and requests for materials should be addressed to Geraldine Seydoux (gseydoux@jhmi.edu).

Author Contributions A.P, M.C, J.S, and G.S designed the research. A.P and M.C. performed all experiments, collected, and analyzed data. G.S and A.P prepared the manuscript with contributions from all authors.

The authors declare no competing interests.

P granules were the first cytoplasmic RNA granules reported to display liquid-like behaviors [11]. P granules are roughly round, can fuse with each other, and exchange components with the cytoplasm. P granules are perinuclear during most of germline development and become cytoplasmic over the oocyte-to-embryo transition [12]. During the first embryonic cell cycle, P granules disassemble and re-assemble in the germ plasm, a region of cytoplasm in the posterior of the embryo that is partitioned to the germ lineage [11]. Several proteins have been implicated in P granule assembly. The RGG-domain protein PGL-3 and its paralog PGL-1 form a core condensate[13,14] that is recruited to the granules by the helicases LAF-1 and GLH-1 and the intrinsically-disordered protein DEPS-1[13,15–17]. Assembly in germ plasm also requires two additional intrinsically-disordered proteins: MEG-3 and its paralog MEG-4[18,19]. Lattice light sheet microscopy of P granules in live wild-type embryos revealed that MEG-3 localizes to a structured phase enriched at the periphery of a more amorphous PGL-3-containing core, raising the possibility that P granules contain multiple phases with distinct material properties[19].

Here we have investigated the dynamic properties of PGL-1, PGL-3, LAF-1, GLH-1, DEPS-1, and MEG-3. We find that while several exhibit liquid-like properties, MEG-3 behaves uniquely like a gel-like polymer. We reconstituted a minimal P granule *in vitro* using MEG-3 and PGL-3, and find that MEG-3 forms gel-like condensates that associate with and stabilize liquid PGL-3 droplets.

RESULTS

P granule proteins exhibit distinct dynamics

To examine P granule protein dynamics in live embryos, we used lines where the *meg-3*, *pgl-1, pgl-3, glh-1, deps-1,* or *laf-1* loci were tagged with GFP or mCherry using CRISPR genome editing (Supplementary Table 1). In wild-type, all 6 fusions enriched in condensates that localize to the posterior end of the one-cell embryo before the first division (Fig. 1a). In embryos where MEG-3 and its paralog MEG-4 were depleted by RNAi or deleted by genome editing, all fusions became delocalized, and were distributed throughout the cytoplasm diffusely and in small condensates (PGL-1, PGL-3, GLH-1, and LAF-1) or in intense bright condensates (DEPS-1) (Fig. 1a, Supplemental Videos 1 and 2). These observations confirm that MEG-3 and MEG-4 are essential to assemble P granules in germ plasm.

To determine rates of granule to cytoplasm exchange, we used fluorescence recovery after photobleaching (FRAP). As reported previously, PGL-1 and GLH-1 exhibited high rates of exchange (Fig. 1b, Supplementary Fig. 1a,b), consistent with co-localization in a liquid phase [11,20]. We found that PGL-3 and LAF-1 also exhibited high rates of exchange (Fig. 1b, Supplementary Fig. 1a,b). We could not detect any exchange for DEPS-1 (Supplementary Fig. 1b), but the relatively low levels of DEPS-1 on granules may have prevented detection of a low exchange rate. MEG-3 exhibited slow exchange dynamics (Fig. 1b, Supplementary Fig. 1a), an order of magnitude slower than PGL-1, PGL-3 and GLH-1, and two orders of magnitude slower than LAF-1 (Table 1). MBK-2 is a kinase that phosphorylates MEG-3 at the oocyte-to-embryo transition to promote P granule dissolution in zygotes [19,21]. We found that MEG-3 dynamics decreased in embryos depleted of MBK-2 by RNAi (Fig. 1b,

Supplementary Fig. 1h). In arrested oocytes, where MBK-2 is not active, we detected no MEG-3 exchange over the time scale tested (Fig. 1b, Supplementary Fig. 1c). In contrast, PGL-1 and PGL-3 dynamics could still be detected in oocytes and were not affected by loss of MBK-2 (Fig. 1b, Supplementary Fig. 1c,e,g,i). PGL-1 dynamics, however, increased significantly in embryos lacking MEG-3 and MEG-4 (Fig. 1b, Supplementary Fig. 1j). We conclude that P granules contain at least two phases with distinct properties: a MEG-3 phase that becomes weakly dynamic in the transition from oocytes to embryos, and a constitutively dynamic, possibly liquid, PGL-containing phase that requires MEG-3 and MEG-4 for localization and stable assembly in embryos.

The MEG-3 phase is gel-like

Liquid phases are often more sensitive to changes in temperature and concentration than solid phases[22,23]. To test the effect of temperature, we filmed embryos co-expressing PGL-3::mCherry and MEG-3::GFP while subjecting them to rapid temperature shifts using a temperature-controlled stage. An up-shift from 20°C (normal growth temperature) to 34°C caused PGL-3::mCherry to dissolve into the cytoplasm within seconds (Fig. 2). Return to 20°C caused PGL-3::mCherry to reappear on the granules after ~ 8 min (Fig. 2). MEG-3::GFP, in contrast, remained in granules throughout the experiment. A longer 15 minute shift to 34°C also did not affect MEG-3::GFP distribution (Supplementary Fig. 2a). These distinct behaviors were not specific to the fluorescent tags as PGL-1::GFP also dissolved immediately when shifted to 34°C, whereas MEG-3::mCherry remained in granules (Supplementary Fig. 2b). To test the effect of concentration, we punctured the eggshell of the embryo with a laser to release cellular contents into an aqueous buffer (Fig. 3a). Consistent with a liquid phase, PGL-3::mCherry diffused immediately upon dilution into the buffer. MEG-3::GFP, in contrast, persisted in the granule phase, as the granules flowed out of the embryo into the dilute buffer (Fig. 3b and Supplemental Video 3). On average, 64 ± 18% of MEG-3::GFP fluorescence remained in the granule phase after extrusion (Fig. 3b). The extruded MEG-3::GFP granules persisted in buffer for at least an hour (Supplementary Fig. 2c). MEG-3::GFP granules remained stable when extruded into buffer containing 1M NaCl, 1,6 hexanediol (5%), or ATP, chemicals that dissolve liquid phases [24,25] (Fig. 3b). MEG-3::GFP granules, however, dissolved in SDS (0.5%) (Fig. 3b). PGL-3::mCherry dissolved in all buffers (Fig. 3b). These observations suggest that the MEG-3 phase is not an irreversible aggregate, but a stable, gel-like phase. In contrast, the PGL-3 phase behaves like a liquid.

The distinct behaviors of MEG-3 and PGL-3 were not specific to the tags (Supplementary Fig. 2d). PGL-1 and GLH-1 behaved like PGL-3 in the diffusion and extrusion assays (Supplementary Fig. 3a–c). LAF-1 and DEPS-1 each exhibited a unique set of behaviors (Supplementary Fig. 3a–c), but neither behaved as stably as MEG-3 in both assays (Table 1).

In vitro reconstitution of a minimal P granule

To determine whether the distinct properties of MEG-3 and PGL-3 observed *in vivo* are intrinsic to these proteins, we generated condensates *in vitro* using purified MEG-3 and PGL-3 (Supplementary Fig. 4a and Methods). Recombinant MEG-3 and PGL-3 were previously shown to phase separate with RNA under pH and salt conditions in the

physiological range [18,26]. For all assays here, we used 0.15 μM MEG-3, 1.8 μM PGL-3, and 0.3 μM of total *C. elegans* RNA, concentrations that respect the proportions of these components in embryos (Methods). To visualize each protein, we labeled a subset of MEG-3 and PGL-3 molecules with Dylight488 or Alexa647 respectively (Methods). As reported previously, when incubated separately in condensate buffer, MEG-3 and PGL-3 readily formed condensates (Fig. 4a). MEG-3 formed small condensates that ceased to grow almost immediately after a short assembly period (<1 min) (Fig. 4a–c, Supplementary Fig. 4b,c). The number and intensity of MEG-3 condensates remained stable over 30 minutes after assembly (Fig. 4b,c). Consistent with a non-dynamic phase, FRAP analyses revealed no exchange between MEG-3 condensates and the dilute phase, even when assayed within ~1 min of condensate formation, the earliest time we could access experimentally (Fig. 4d). In contrast, PGL-3 formed dynamic condensates (k_{rec}^{PGL-3} = 0.037 ± 0.001 s^{-1}, Fig. 4d, Supplementary Fig. 4d, and [26]), that increased in intensity and decreased in number over time, as expected for a liquid phase growing by Ostwald ripening and fusion (Fig. 4a–c, Supplementary Fig. 4b,c). When introduced together in condensate buffer, MEG-3 and PGL-3 initially formed separate condensates (1 min) (Fig. 4a, Supplementary Fig. 4e). By 5 minutes of incubation, we begin to observe co-assemblies and by 30 minutes the majority of condensates contained both MEG-3 and PGL-3 (Fig. 4a, Supplementary Fig. 4e). During this period, the MEG-3 and PGL-3 condensates increased in intensity and decreased in number, as observed for PGL-3-only condensates (Fig. 4b,c). At early co-assembly time points, we could observe one or more distinct MEG-3 condensates on the surface of a PGL-3 droplet (Fig. 4a,e). By 30 minutes, more MEG-3 condensates accumulated around the PGL-3 phase (Fig. 4a,e and Supplementary Fig. 4f). In the co-condensates, the PGL-3 phase maintained rapid exchange with the surrounding dilute phase, as observed in PGL-3-only condensates (Fig. 4d). In contrast, we observed no exchange in the MEG-3 phase (Fig. 4d). The MEG-3 condensates, however, appeared to move relative to each other on the PGL-3 surface and the co-condensates could fuse (Supplementary Fig. 4g–i, Supplemental Videos 4–6). These observations suggest that the MEG-3 condensates do not interfere significantly with the liquid dynamics of the PGL phase.

To determine whether P granule assembly *in vivo* also involves interactions between MEG-3 and PGL-3 condensates, we imaged P granules in live embryos. In 1 and 2-cell embryos, we observed PGL-3 condensates surrounded by multiple, discrete smaller MEG-3 condensates (Figure. 4e, Supplementary Fig. 5a). By the 4-cell stage, most PGL-3 droplets were surrounded by an uneven MEG-3 layer (Figure. 5e, Supplementary Fig. 5b), as described previously[19]. Consistent with smaller MEG-3 condensates coalescing onto larger PGL-3 droplets, MEG-3 forms smaller granules in embryos lacking PGL-1 and PGL-3[18,19]. We conclude that co-assembly of PGL and MEG phases *in vitro* and *in vivo* involves accumulation of multiple MEG-3 condensates around growing PGL-3 droplets.

MEG-3 condensates stabilize PGL-3 condensates

As observed for MEG-3 *ex vivo*, MEG-3 condensates assembled *in vitro* were resistant to 1M NaCl, 7 mM ATP, partially resistant to 5% 1,6 hexanediol, and sensitive to 0.5% SDS. PGL-3 condensates, in contrast, were sensitive to all these reagents (Fig. 5a,b, Supplementary Fig. 6a–d). In the co-condensates, MEG-3 showed the same range of

resistance as in the single condensates and PGL-3 became partially resistant to 1M salt, 7 mM ATP and 5% 1,6 hexanediol. The effect was most striking with 1M NaCl. PGL-3 condensates dissolve almost completely in 1M NaCl, but persisted partially in the co-condensates. After a 15-minute incubation in 1M NaCl, the co-condensates became "hollow", losing most of the PGL-3-rich core, but retaining some PGL-3 foci in the MEG-3 ring. (Fig. 5a,b, Supplementary Fig. 6b). We conclude that, as observed *in vivo*, the MEG-3 phase stabilizes the PGL-3 phase.

The intrinsically disordered N-terminal domain of MEG-3 is not sufficient to form gel-like condensates

MEG-3 contains a long (~600 amino acids) predicted intrinsically-disordered region (IDR) at its N-terminus, and a shorter, predicted ordered domain at its C-terminus. When expressed on its own from the *meg-3* locus, the MEG-3 IDR localizes to the germ plasm but is not sufficient to support granule formation under normal conditions [18]. We showed previously that the IDR readily phase separates *in vitro* at concentrations greater than 1 μM [18]. We found, however, that at 0.15 μM, the MEG-3 IDR does not form visible condensates even in the presence of RNA (Fig. 5b, Supplementary Fig. 6a). When mixed with RNA and PGL-3, the MEG-3 IDR was recruited into the PGL-3 condensates (Fig. 5b, Supplementary 6a), but did not form a distinct phase. Instead, the MEG-3 IDR distributed evenly throughout the PGL-3 condensate. MEG-3 IDR and PGL-3 co-condensates dissolved in 1M NaCl, as do PGL-3-only condensates (Fig. 5a,b). We conclude that formation of a stabilizing scaffold requires the MEG-3 C-terminus *in vitro*, as it does *in vivo*.

DISCUSSION

P granules were the first RNA granules proposed to be liquid droplets formed by liquid-liquid phase separation (LLPS)[11]. The demonstration that certain P granule proteins undergo LLPS spontaneously *in vitro* lent support to this hypothesis [17,26], but the mechanisms that favor LLPS in the posterior of the embryo were not clear. A competition for RNA between PGL-3 and MEX-5, an RNA-binding protein enriched in the anterior[26], was proposed as a possible mechanism, but this model did not account for the role of MEG-3[18,27]. Our findings here suggest that the unique properties of the MEG-3 phase are what drives preferential LLPS of P granule proteins in the posterior cytoplasm (Fig. 6). MEG-3 forms stable, gel-like condensates that recruit PGL-3 molecules and associate with liquid PGL-3 droplets. In the co-condensates, the MEG-3 phase stabilizes the PGL-3 phase while maintaining the liquid dynamics necessary for granule growth. In embryos, posterior-enriched MEG-3 is required both for assembly of P granules in the posterior and disassembly of P granules in the anterior[18]. Our *in vitro* findings provide an explanation for this phenomenon: because the PGL phase remains in dynamic equilibrium with the cytoplasm in the co-condensates, stimulation of PGL condensation by posterior-enriched MEG-3 creates a posterior-directed flux of PGL molecules that destabilizes PGL droplets in the anterior cytoplasm. Artificial seeds that concentrate components of liquid phases are sufficient to promote LLPS in cells[28]. We suggest that the gel-like MEG-3 condensates function as biological seeds for P granules in the *C. elegans* germ plasm. Non-dynamic gel-like cores have been reported in biomolecular condensates [9,10,29], but their significance has been debated. Our findings

suggest that gel-like polymers are essential structural elements of biomolecular condensates that stimulate LLPS by increasing the local concentration of key components of liquid phases.

Online Methods

Materials and Methods

Strain maintenance and RNA-mediated interference—*C. elegans* was cultured according to standard methods at 20°C unless otherwise stated [30]. Genome editing was performed using CRISPR/Cas9 as previously described [31]. Strains used in this study are listed in Table S1.

mbk-2 or *meg-3meg-4 (RNAi)* was performed by feeding [32] using plasmids from the Ahringer or Openbiosystems libraries. HT115 bacteria transformed with feeding vectors were grown at 37°C in LB + ampicillin (100 μg/ml) for 5 hr, induced with 5 mM IPTG for 45 min, plated on NNGM (nematode nutritional growth media) + ampicillin (100 μg/ml) + IPTG (1 mM), and grown overnight at room temperature. For *mbk-2 RNAi,* embryos were hatched on RNAi plates and allowed to feed for ~3–4 days. For *meg-3meg-4 RNAi*, L4 larvae were fed at 20°C for 24–40 hr.

For visualization of arrested oocytes, *fog-2 (q71)* females, which do not produce sperm, were collected in the L4 stage and matured for 8 hours before imaging in 20 nM levamisole. For imaging of embryos, adult hermaphrodites were dissected in 1X *ex vivo* buffer (25 mM HEPES pH 7, 150 mM NaCl, 2 mM $CaCl_2$, 2 mM $MgCl_2$) to release embryos which were mounted onto 2% agarose pads on glass slides.

Microscopy: Images shown in Fig. 1, 2, 3, 4a,e (left panel), and 5, Extended Data Fig. 1, 2, 3, 5b,g,h, 6, 7 were captured with a Zeiss Axio Imager equipped with a Yokogawa spinning-disc confocal scanner and Slidebook v 6.0 software (Intelligent Imaging Innovations). Unless otherwise noted embryo and oocyte images are Z stack maximum projections using a Z step size of 1 μm, spanning the depth of the oocyte or embryos using a 60x objective. *In vitro* granule images or videos are single planes taken using a 60x objective (Fig. 4a,e, 5a,b, Extended Data Fig. 4b, 6a,b, 7) or 40x objective Extended Data Fig. 4g,h, Supplemental Videos 4,5). Images shown in Fig. 4e (right panel) and Extended Data Fig. 5 were captured with a GE OMX-SR microscope with Aquire SR software and deconvoluted with softWoRx software. Embryo images are Z stack maximum projections using a Z step size of 0.125 μm, spanning the depth of the embryo. Images of enlarged granules are single planes. Images were acquired using 90ms exposures in the 488 channel and 65ms exposures in the 561channel using a 60x objective. Images shown in Fig. 4d, Extended Data Fig. 4d,i, and Supplemental Video 6 were captured with using a Zeiss LSM 800 GaAsp system. Images are single confocal planes imaged using a 63x objective every 1–3s during a recovery phase of 300s with a laser power of 0.3%−0.5% and a gain of 600–700. All image analyses were conducted using the Fiji image-processing package (http://fiji.sc/Fiji).

Fluorescence Recovery after Photobleaching (FRAP)

In vivo: Photobleaching of P granule proteins in oocytes or embryos was performed using a laser to bleach a region slightly larger than the area of the granule (2 μm diameter) in the center plane of the Z-stack. Images were acquired as Z-stacks with 10 planes with a step size 1 μm (oocytes) or 11 planes with a step size of 0.6 μm (embryos) by imaging 50 ms exposures for all proteins in oocytes and MEG-3::GFP, LAF-1::GFP, DEPS-1::GFP in embryos, 25 ms exposures for PGL-3::mCherry, PGL-1::GFP, GLH-1::GFP in embryos, and 300 ms exposures for MEG-3::mCherry in embryos using a 63x objective. In oocytes, images were acquired every 5s. In embryos, images were acquired every 3s (PGL-1::GFP, GLH-1::GFP, LAF-1::GFP),5s (MEG-3::GFP, DEPS-1::GFP, PGL-3::mCherry), or 7s (MEG-3::mCherry) during a recovery phase of 180–300s after photobleaching.

In vitro: 20 μL condensation reaction (prepared as described below) were added to a chambered coverglass (Grace BioLabs) and imaged using a Zeiss LSM 800 GaAsp system. Bleaching was performed using 100% laser power in the 488 and 647 channels for MEG-3-Dylight 488 or PGL-3-Alexa 647 respectively. Regions of slightly larger than the condensates (radius ≈ 2.5 μM) or regions within condensates (radius ≈ 1 μM) were photobleached. A single confocal plane was imaged using a 63x objective every 3s during a recovery phase of 300s with a laser power of 0.3%−0.5% and a gain of 600–700.

Maximum projections of Z-stacks acquired as above were analyzed in Fiji. The total or mean fluorescence intensity of the area containing the granule was measured at each time point. Fluorescence recovery was corrected for background and normalized to the initial granule intensity using the equation: $nI = (I\text{-}I^{bkg})/(I^{i}\text{-}I^{bkgi})$, where nI is the background corrected and normalized fluorescence intensity, I is the intensity of the FRAPed granule, I^{bkg} is the fluorescence intensity of the unFRAPed cytoplasm, I^{i} is the initial intensity of the FRAPed granule before bleaching, and I^{bkgi} is the initial background intensity. For *in vitro* FRAP, the normalized intensity was corrected for photobleaching using the average photobleaching rate calculated from unFRAPed condensates in the imaging area. Photobleaching was minimal in embryos and oocytes over the time course of the experiment (<10%) except for LAF-1::GFP. For the LAF-1 experiments, the normalized intensity was corrected for photobleaching using the average photobleaching rate from an unFRAPed region of the cytoplasm in the imaging area. Recovery rates were determined by fitting individual traces to a first order equation $nI = (A^{rec}\cdot(1\text{-}e^{-\boldsymbol{kt}})$. Where A^{rec} is the fluorescence recovery amplitude and $\boldsymbol{k}$ is the rate of fluorescence recovery. For MEG-3::GFP FRAP experiments in *mbk-2 (RNAi)* embryos where amplitudes only just approached full recovery during the time frame of the experiment, final recovery amplitudes were limited to $A^{rec} = 1$.

Temperature shifts: Temperature shift experiments were performed on a fluidic temperature control stage which enabled rapid temperature shifts (CherryTemp™, CherryBiotech). Embryos were prepared as described for FRAP experiments. Images were acquired using a z step size of 1μm, spanning the entire depth of the embryo. Final images are Z-stack maximum projections. Images were taken every 15s broken into the following segments: 1 min at 20°C followed by a 3–15 min shift to 34°C and then returned to 20°C for 25 min.

***Ex vivo* Experiments—**All *ex vivo* buffers were prepared in 25 mM HEPES pH 7, 150 mM NaCl, 2 mM $CaCl_2$, 2 mM $MgCl_2$ buffered to pH 7.0 with NaOH and HCl using a Mettler Toledo Seveneasy pH meter and a Fisherbrand™ Accumet™ glass body standard combination mercury free electrode. Embryos were dissected from adult hermaphrodites in *ex vivo* buffer and mounted on glass slides with 3% agarose pads made with 1X *ex vivo* buffer. Embryo contents were extruded by puncturing the eggshell near the anterior region of the germline blastomere using a 3i Ablate!™ laser system at 532 nm pulse setting with a power level of 155. All embryo images are Z stack maximum projections using a Z step size of 1 μm, spanning the entire depth of the embryo. Images were acquired using 50 ms exposures in the 488 channel and/or 50 ms exposures in the 561 channel every 10s using a 63x objective. For MEG-3::mCherry, the 561 laser power was reduced to 50% and 300 ms exposures were taken due to low fluorescence signal. For Extended Data Fig. 2c, images were taken every 15 min for 60 min following extrusion.

To quantify MEG-3::GFP persistence in granules, photomicrographs acquired as described above were analyzed using ImageJ64. Background was subtracted from each image using a rolling ball radius of 50 pixels. Pixels were smoothed 1 time and images were converted to 8-bit. The pixel brightness threshold was set to 50–255 and the total integrated density of the objects (MEG-3::GFP granules) was quantified. Total fluorescence intensity was calculated before (I_B) and after (I_A) extrusion and used to calculate a fluorescence ratio (I_A/I_B). For some embryos, granules left the field of view and could not be counted. The I_A /I_B, therefore, is a minimal estimate of the fraction of MEG-3::GFP that remains in the granule phase after extrusion.

Protein purification and labeling

Overview: MEG-3 was purified from E. coli under denaturing conditions as a His-tagged fusion or under native conditions as an MBP fusion followed by protease removal of MBP (Extended Data Fig. 4a). No significant differences were noted between the two purification methods. PGL-3 was purified from E. coli as an MBP fusion followed by protease removal of MBP (Extended Data Fig. 4a).

Purification of MEG-3 His-tagged fusion: MEG-3 full-length (aa1–862) and MEG-3_{IDR} (aa1–698) fused to an N-terminal 6XHis tag in pET28a were expressed and purified from inclusion bodies using a denaturing protocol as described [18].

Purification of MBP fusions: MBP-TEV-PGL-3 or MBP-TEV-MEG-3 were expressed in Rosetta (DE3) cells at 16°C in terrific broth + ampicillin (100 μg/mL) to an OD600 of ~1.0 and induced with 1 mM isopropyl β-D-1-thiogalactopyranoside at 16° C for 16 hr. Cells were resuspended in Buffer A (25 mM HEPES pH 7.4, 500 mM NaCl, 0.4 M L-Arginine, 20% (vol/vol) glycerol, 1 mM DTT) with added protease inhibitors, 5 μg/mL RNase A (USB), 0.25 U/μL RNase I (Ambion), lysed by sonication, spun at 13,000 rpm for 15 min. Lysates were filtered and passed over a MBPTrap column (GE Healthcare). The resin was washed with Buffer B1000 (25 mM HEPES pH 7.4, 40% (vol/vol) glycerol, 1 mM DTT, 1000 mM NaCl). Protein was eluted in Buffer B1000 + 20 mM Maltose. Solutions were diluted 2-fold with Buffer B with 0 mM NaCl (B0) for a final concentration of 500 mM

NaCl. 400 units of ProTEV protease (Promega) was added per mg of protein for 2–4hr at RT to remove the MBP tag. Solutions were diluted to 200 mM NaCl with Buffer B0, and immediately loaded onto a HeparinTrap column (GE Healthcare). Proteins were washed and eluted with a stepwise gradient made by mixing Buffer B0 with B1000. Untagged PGL-3 and MEG-3 were eluted in 500 or 800 mM NaCl respectively. Protein containing fractions were flash frozen in small aliquots in liquid nitrogen, and stored at −80 °C.

Protein labeling: Proteins were labeled with succinimidyl ester reactive fluorophores from Molecular Probes (Alexa Fluor™ 647 NHS or DyLight™ 488 NHS Ester) following manufacturer instructions. Free fluorophore was eliminated by passage through three Zeba™ Spin Desalting Columns (7K MWCO, 0.5 mL) into protein storage buffer. The concentration of fluorophore-labeled protein was determined using fluorophore extinction coefficients. Labeling reactions resulted in ~ 0.25–1 label per protein. Aliquots were snap frozen and stored. In phase separation experiments, fluorophore-labeled protein was mixed with unlabeled protein for final reaction concentrations of 25–100 nM of fluorophore.

RNA preparation—Total RNA was extracted from a *C. elegans* culture using TRIzol (Invitrogen) following published methods. poly-A selected RNA was prepared using Dynabeads™ Oligo$(dT)_{25}$ (ThermoFisher) using two rounds of selection.

***In vitro* condensation experiments—**Protein condensation was induced by diluting proteins out of storage buffer into condensation buffer containing 25 mM HEPES (pH 7.4), NaCl adjusted to a final concentration of 150 mM, and RNA. For experiments shown in Fig. 4,5 and Extended Data Fig. 4,6 total ceRNA was denatured at 95°C for 30s and added to the condensation buffer to a final concentration of 150 ng/μL. For data included in Fig. 5b, Extended Data Fig. 6c,d, replicates included poly-A selected RNA used at a concentration of 150 ng/μL.

The concentrations of MEG-3, PGL-3 and mRNA have been estimated at 11 ± 4 nM, 680 ± 200 nM and 100 nM (50 ng/μL), respectively [26]. These estimates were derived from pooled, mixed-stage embryos and thus are likely to be underestimates for MEG-3 and PGL-3, since these proteins are concentrated in just one cell per embryo, and are not present after the 100-cell stage in the case of MEG-3. We tested a range of concentrations in co-assembly experiments and found that MEG-3/PGL-3 condensates form over a wide range of concentrations as long as the ratio of RNA to MEG-3 is kept high to prevent co-assemblies of PGL-3 and MEG-3 from aggregating (Extended Data Fig. 7). Unless otherwise indicated, for all co-assembly experiments, we used 150 nM MEG-3/MEG-3-Dylight488, 1.8 μM PGL-3/PGL-3-Alexa647 and 300 nM (150 ng/μL) RNA. Altering the order of addition did not affect co-condensate assembly. Condensation reactions were incubated at room temperature for 30 min or less as indicated, before spotting onto thin chambered glass slides (ERIE SCIENTIFIC COMPANY 30–2066A) with a coverslip. Condensates were imaged using a Zeiss Axio Imager equipped with a Yokogawa spinning-disc confocal scanner and Slidebook v 6.0 software (Intelligent Imaging Innovations). Images used for quantification are single planes acquired using a 40x oil objective over an area spanning 171 × 171 μm^2. For Supplemental Videos 4–6 slides were treated with PEG-silane [33].

To quantify the ratio of MEG-3-Dylight or PGL-3-Alexa647 in condensates, a mask was created by thresholding images, filtering out objects of less than 2 pixels to minimize noise, and applying a watershed filter to improve separation of condensates close in proximity, and converted to a binary image by the Otsu method using the nucleus counter cookbook plugin in FIJI. Minimum thresholds were set to the mean intensity of the background signal of the image. The maximum threshold was calculated by adding 2 times the standard deviation of the background. To develop a mask to measure co-condensate assembly, individual channels of MEG-3-Dylight488 and PGL-3-Alexa647 images were set to thresholds as described above and averaged. The resulting image was processed as described above to generate the co-condensate mask. Using generated masks, the integrated intensity within each condensate was calculated. To remove non-specific background signal the mean intensity of an image field in the absence of the labeled protein was subtracted from each pixel yielding the total intensity of each condensate. To calculate the ratio in condensates, the sum of intensities of all condensates in an imaged area (I_C) was divided by the total intensity of the imaged area (I_T). Each data point represents data from 4 images acquired in a single experiment.

To quantify co-localization of MEG-3 and PGL-3 in co-condensates over time, the covariance of MEG-3 and PGL-3 intensity within condensates measured using the co-condensate mask were compared using the Pearson's correlation coefficient. Data points represent the mean ± SD of coefficients calculated for a total of 16 images from 4 experimental replicates.

Radial profile plot—To quantify the heterogeneity of the MEG-3 and PGL-3 phases of the condensates, a radial profile plot was generated using the oval profile plugin in ImageJ64. A region centered on and slightly larger than the condensate was drawn. The maximum intensity of radii extending from the center of the region to the exterior in 3 degree increments was calculated, the mean background was subtracted and intensities were normalized to the maximum intensity and plotted for PGL-3 and MEG-3. The resulting plot shows the variation in intensity around the circumference of the condensate.

Graphing and data fitting—All data was plotted and statistical analysis was conducted using Graphpad Prism 7 software. Fitting of recovery curves in FRAP experiments was conducted using Kaleidagraph (Synergy) software.

Data Availability—Source data for Figs. 1, 3–5 and Supplemental Fig. 3 are available with the paper online. Other data supporting the findings of this study are available from the corresponding author upon reasonable request.

Supplementary Material

Refer to Web version on PubMed Central for supplementary material.

Acknowledgments

We thank Dominique Rasoloson who provided strains JH3269 and Helen Schmidt who provided strain JH3606, and Andrew Folkmann for comments on the manuscript. Some strains were provided by the CGC, which is funded by NIH Office of Research Infrastructure Programs (P40 OD010440). Data acquired using the Zeiss LSM 800 Confocal reported in this publication was supported by Office of the Director, NIH (OD) of the National Institutes

of Health (award number S10OD016374). This work was supported by the National Institutes of Health (NIH) (grant number R37 HD37047, G.S.). M.C. was supported by a training grant T32 GM007445 and NSF Graduate Research Fellowship DGE-1746891. G.S. is an investigator of the Howard Hughes Medical Institute.

References

1. Hyman AA, Weber CA & Julicher F Liquid-liquid phase separation in biology. Annu Rev Cell Dev Biol 30, 39–58, doi:10.1146/annurev-cellbio-100913-013325 (2014). [PubMed: 25288112]
2. Boeynaems S et al. Protein Phase Separation: A New Phase in Cell Biology. Trends Cell Biol 28, 420–435, doi:10.1016/j.tcb.2018.02.004 (2018). [PubMed: 29602697]
3. Shin Y & Brangwynne CP Liquid phase condensation in cell physiology and disease. Science 357, doi:10.1126/science.aaf4382 (2017).
4. Han TW et al. Cell-free formation of RNA granules: bound RNAs identify features and components of cellular assemblies. Cell 149, 768–779, doi:10.1016/j.cell.2012.04.016 (2012). [PubMed: 22579282]
5. Kato M et al. Cell-free formation of RNA granules: low complexity sequence domains form dynamic fibers within hydrogels. Cell 149, 753–767, doi:10.1016/j.cell.2012.04.017 (2012). [PubMed: 22579281]
6. Lin Y, Protter DS, Rosen MK & Parker R Formation and Maturation of Phase-Separated Liquid Droplets by RNA-Binding Proteins. Mol Cell 60, 208–219, doi:10.1016/j.molcel.2015.08.018 (2015). [PubMed: 26412307]
7. Molliex A et al. Phase separation by low complexity domains promotes stress granule assembly and drives pathological fibrillization. Cell 163, 123–133, doi:10.1016/j.cell.2015.09.015 (2015). [PubMed: 26406374]
8. Taylor JP, Brown RH Jr. & Cleveland DW Decoding ALS: from genes to mechanism. Nature 539, 197–206, doi:10.1038/nature20413 (2016). [PubMed: 27830784]
9. Jain S et al. ATPase-Modulated Stress Granules Contain a Diverse Proteome and Substructure. Cell 164, 487–498, doi:10.1016/j.cell.2015.12.038 (2016). [PubMed: 26777405]
10. Wheeler JR, Matheny T, Jain S, Abrisch R & Parker R Distinct stages in stress granule assembly and disassembly. Elife 5, doi:10.7554/eLife.18413 (2016).
11. Brangwynne CP et al. Germline P granules are liquid droplets that localize by controlled dissolution/condensation. Science 324, 1729–1732, doi:1172046 [pii] 10.1126/science.1172046 (2009). [PubMed: 19460965]
12. Strome S Specification of the germ line. WormBook, 1–10, doi:10.1895/wormbook.1.9.1 (2005).
13. Hanazawa M, Yonetani M & Sugimoto A PGL proteins self associate and bind RNPs to mediate germ granule assembly in C. elegans. Journal of Cell Biology 192, 929–937, doi:jcb.201010106 [pii] 10.1083/jcb.201010106 (2011). [PubMed: 21402787]
14. Kawasaki I et al. The PGL family proteins associate with germ granules and function redundantly in Caenorhabditis elegans germline development. Genetics 167, 645–661 (2004). [PubMed: 15238518]
15. Spike C et al. Genetic analysis of the Caenorhabditis elegans GLH family of P-granule proteins. Genetics 178, 1973–1987 (2008). [PubMed: 18430929]
16. Spike CA, Bader J, Reinke V & Strome S DEPS-1 promotes P-granule assembly and RNA interference in C. elegans germ cells. Development 135, 983–993 (2008). [PubMed: 18234720]
17. Elbaum-Garfinkle S et al. The disordered P granule protein LAF-1 drives phase separation into droplets with tunable viscosity and dynamics. Proc Natl Acad Sci U S A 112, 7189–7194, doi:10.1073/pnas.1504822112 (2015). [PubMed: 26015579]
18. Smith J et al. Spatial patterning of P granules by RNA-induced phase separation of the intrinsically-disordered protein MEG-3. Elife 5, doi:10.7554/eLife.21337 (2016).
19. Wang JT et al. Regulation of RNA granule dynamics by phosphorylation of serine-rich, intrinsically disordered proteins in C. elegans. Elife 3, e04591, doi:10.7554/eLife.04591 (2014). [PubMed: 25535836]

20. Sheth U, Pitt J, Dennis S & Priess JR Perinuclear P granules are the principal sites of mRNA export in adult C. elegans germ cells. Development 137, 1305–1314, doi:10.1242/dev.044255 (2010). [PubMed: 20223759]
21. Pellettieri J, Reinke V, Kim SK & Seydoux G Coordinate activation of maternal protein degradation during the egg-to-embryo transition in C. elegans. Dev Cell 5, 451–462 (2003). [PubMed: 12967564]
22. Weber SC & Brangwynne CP Getting RNA and protein in phase. Cell 149, 1188–1191, doi: 10.1016/j.cell.2012.05.022 (2012). [PubMed: 22682242]
23. Banani SF, Lee HO, Hyman AA & Rosen MK Biomolecular condensates: organizers of cellular biochemistry. Nat Rev Mol Cell Biol 18, 285–298, doi:10.1038/nrm.2017.7 (2017). [PubMed: 28225081]
24. Patel A et al. ATP as a biological hydrotrope. Science 356, 753–756, doi:10.1126/science.aaf6846 (2017). [PubMed: 28522535]
25. Lin Y et al. Toxic PR Poly-Dipeptides Encoded by the C9orf72 Repeat Expansion Target LC Domain Polymers. Cell 167, 789–802 e712, doi:10.1016/j.cell.2016.10.003 (2016). [PubMed: 27768897]
26. Saha S et al. Polar Positioning of Phase-Separated Liquid Compartments in Cells Regulated by an mRNA Competition Mechanism. Cell 166, 1572–1584 e1516, doi:10.1016/j.cell.2016.08.006 (2016). [PubMed: 27594427]
27. Seydoux G The P Granules of C. elegans: A Genetic Model for the Study of RNA-Protein Condensates. J Mol Biol 430, 4702–4710, doi:10.1016/j.jmb.2018.08.007 (2018). [PubMed: 30096346]
28. Bracha D et al. Mapping Local and Global Liquid Phase Behavior in Living Cells Using Photo-Oligomerizable Seeds. Cell 175, 1467–1480 e1413, doi:10.1016/j.cell.2018.10.048 (2018). [PubMed: 30500534]
29. Woodruff JB, Hyman AA & Boke E Organization and Function of Non-dynamic Biomolecular Condensates. Trends Biochem Sci 43, 81–94, doi:10.1016/j.tibs.2017.11.005 (2018). [PubMed: 29258725]
30. Brenner S The genetics of Caenorhabditis elegans. Genetics 77, 71–94 (1974). [PubMed: 4366476]
31. Paix A, Folkmann A, Rasoloson D & Seydoux G High Efficiency, Homology-Directed Genome Editing in Caenorhabditis elegans Using CRISPR-Cas9 Ribonucleoprotein Complexes. Genetics 201, 47–54, doi:10.1534/genetics.115.179382 (2015). [PubMed: 26187122]
32. Timmons L & Fire A Specific interference by ingested dsRNA. Nature 395, 854 (1998). [PubMed: 9804418]
33. Alberti S et al. A User's Guide for Phase Separation Assays with Purified Proteins. J Mol Biol, doi: 10.1016/j.jmb.2018.06.038 (2018).

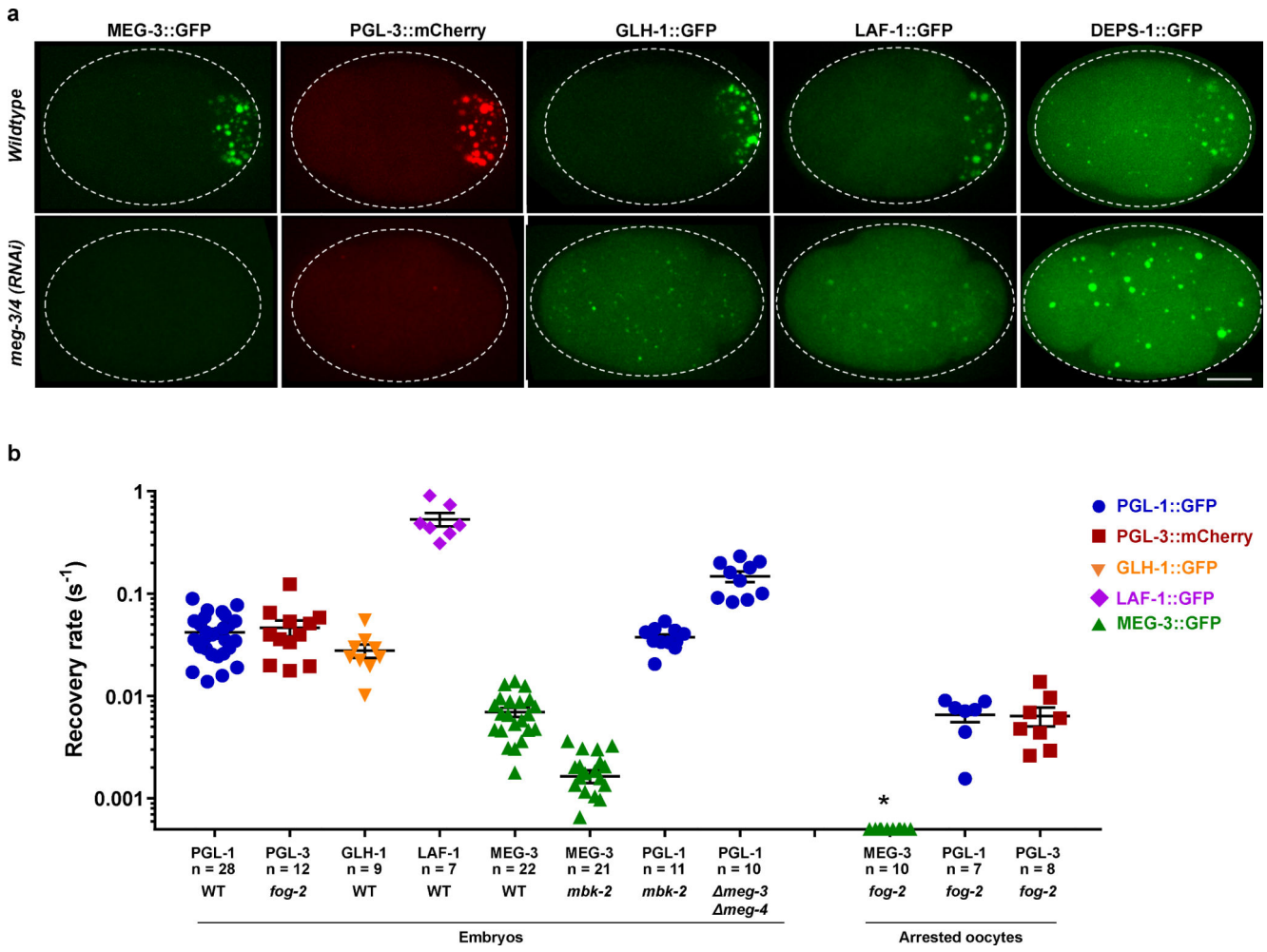

Fig. 1 –. P granule proteins exhibit distinct dynamics

a. Photomicrographs of 4-cell embryos co-expressing tagged MEG-3::GFP and PGL-3::mCherry or expressing single GFP-tagged P granule proteins GLH-1::GFP, LAF-1::GFP, DEPS-1::GFP in wildtype embryos or embryos depleted of MEG-3/4 by RNAi (see Source Data for n values). Scale bar is 10 μm.

b. Graph showing recovery rates from FRAP experiments plotted in Supplementary Fig. 1. Each symbol represents one FRAP experiment on one granule. The rate of fluorescence recovery (Methods) is plotted on the y-axis on a log scale. The x-axis indicates the P granule protein, genotype, and stage tested. *fog-2* is a feminizing mutation used here to arrest oocytes in the absence of sperm. Error bars represent mean ± SEM calculated from independent experiments. n values are indicated in the x-axis label. For data points marked by "*", no recovery was detected. Supplementary Fig. 1 shows recovery curves and photomicrographs of representative FRAP experiments. Source data are available in Supplementary Data Set 1.

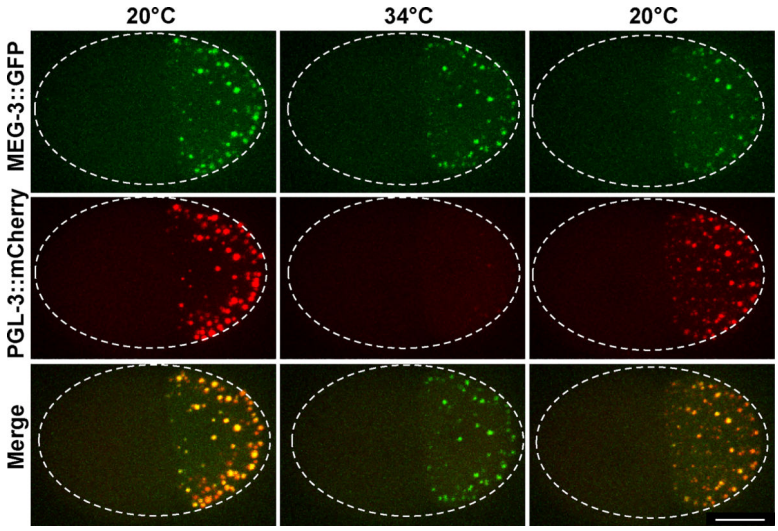

Fig. 2 –. Effect of temperature on the MEG-3 and PGL-3 phases

Time-lapse photomicrographs of a 2-cell embryo co-expressing MEG-3::GFP and PGL-3::mCherry fusions and cultured at 20°C, up-shifted to 34°C for 1 minute, and downshifted back to 20°C for 8 minutes. Scale bar is 10 μm. Images are representative of 6 independent experiments.

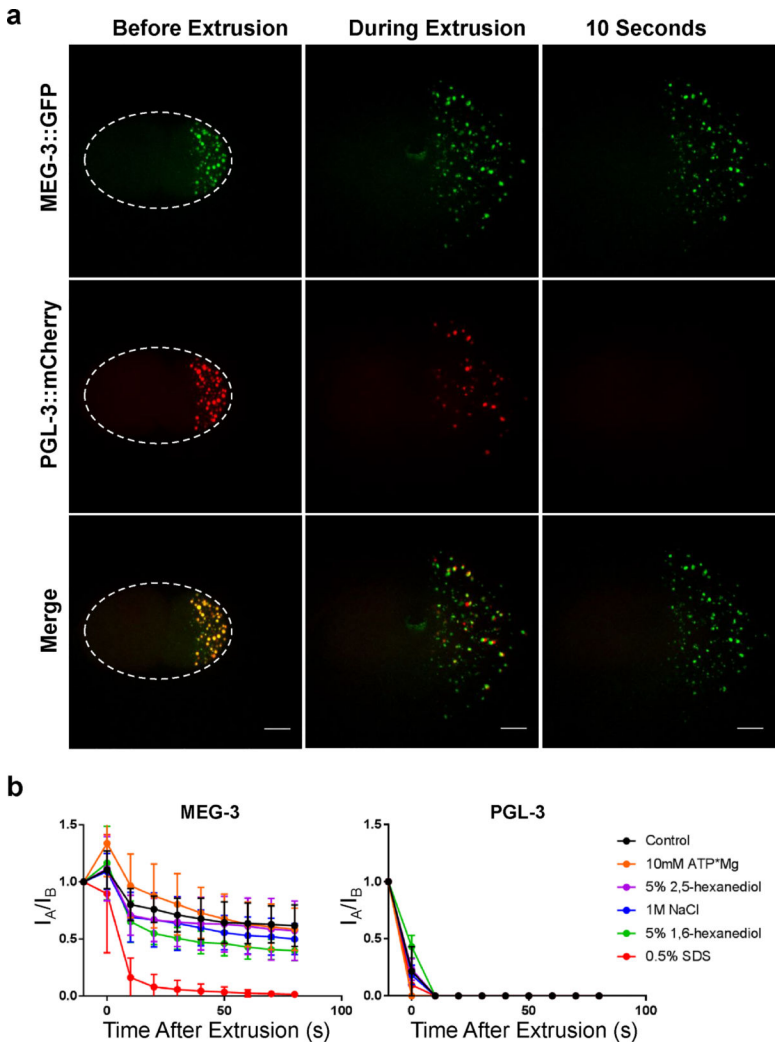

Fig. 3 –. Effect of dilution on the MEG-3 and PGL-3 phases

a. Time-lapse photomicrographs of a 2-cell embryo co-expressing MEG-3::GFP and PGL-3::mCherry fusions before, immediately after (~1s), and 10s after laser puncture of the eggshell. Laser puncture causes the contents of the posterior blastomere to spill onto the slide mixing with the aqueous buffer. Scale bar is 10 μm.

b. Graphs showing the fraction of MEG-3::GFP or PGL-3::mCherry retained in the granular phase after extrusion. Total GFP or mCherry fluorescence from granules was measured before laser puncture (I_B) and after laser puncture (I_A) and used to calculate a fluorescence ratio (I_A/I_B). Means are indicated along with error bars representing ± SD calculated from multiple embryos (see Source Data for n values). Source data for panel b are available in Supplementary Data Set 1.

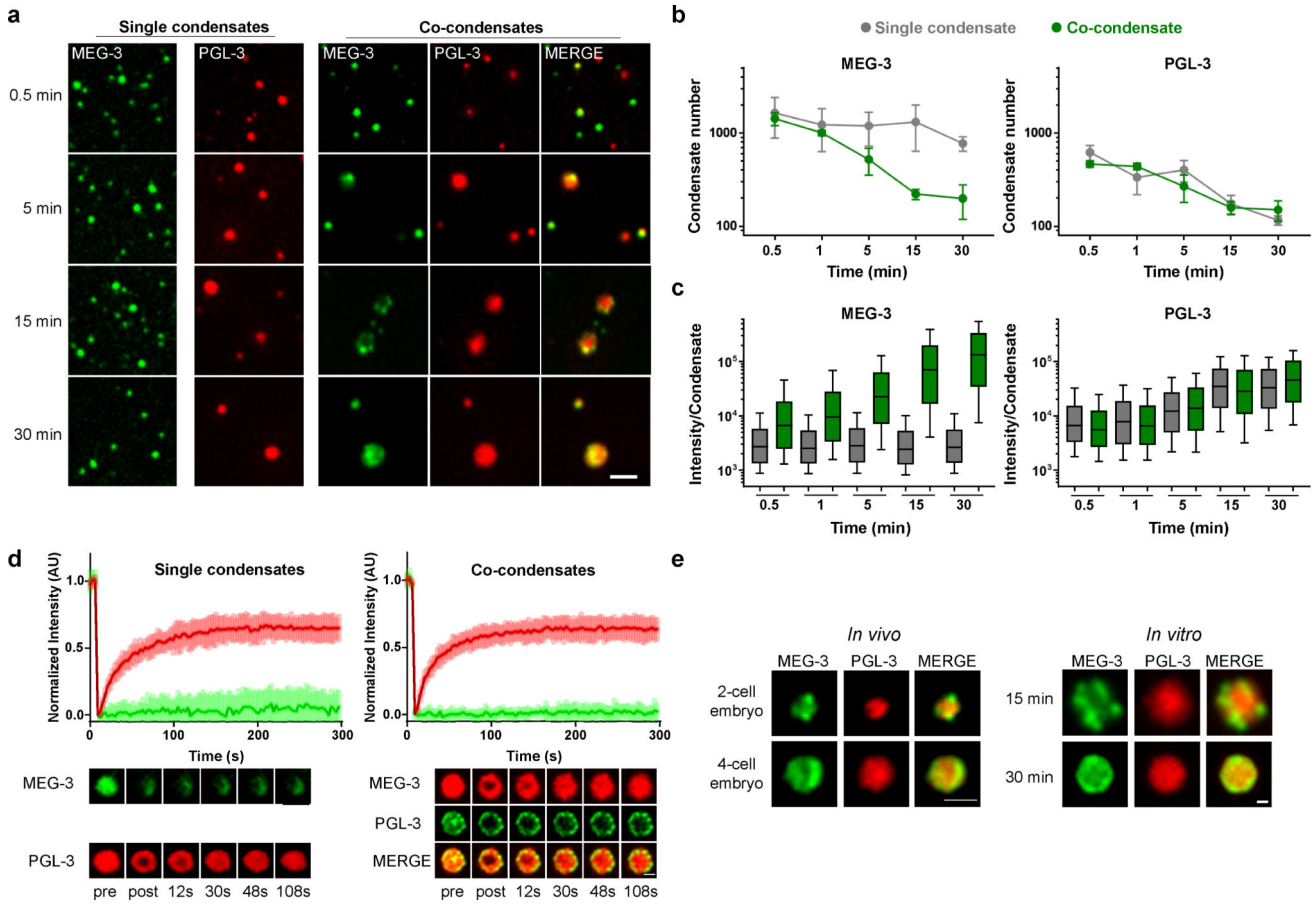

Fig. 4 –. *In vitro* assembly of MEG-3 and PGL-3 condensates

a. Representative photomicrographs of MEG-3 and PGL-3 condensates after incubation in condensation buffer for the indicated times. MEG-3 was trace labeled with Dylight488 (green) and PGL-3 with Alexa647 (red) (Methods). Each image was adjusted separately to optimize visualization of small condensates in the first time point, and condensate substructure in the other time points. See Supplementary Fig. 4b for uniformly processed images. Images are representative of data quantified in b and c. Scale bars are 5 μm.

b. Graphs showing the number condensates of MEG-3 or PGL-3 when incubated singly (gray) or together (green) at increasing time of incubation in condensate buffer. Each data set includes condensates from 16 images collected from 4 experimental replicates. Circles indicate the mean and bars represent the SD.

c. Graphs showing the distribution of total intensity of individual condensates of MEG-3 or PGL-3 when incubated singly (gray boxes) or together (green boxes) at increasing time of incubation in condensate buffer. Each data set includes condensates from 16 images collected from 4 experimental replicates. Black lines indicate the mean, whiskers represent the entire range of the data, and bars represent the 90% confidence interval calculated from >500 condensates for each condition.

d. Graph showing fluorescence recovery after partial photobleaching (FRAP) of condensates assembled as in (**a**) and incubated for 30 min in condensate buffer. Granule intensity of MEG-3 or PGL-3 individual condensates (left panels, n=8) or co-condensates (right panels,

n=7) was measured every 3s for 300s before and after bleaching. Values were normalized to initial fluorescence intensity, corrected for photobleaching and plotted as an average. Error bars represent mean ± SD. Representative images are shown in the bottom panels. Scale bars are 1 μm. See Supplementary Fig. 4d for FRAP of fully bleached PGL-3 droplets.
e. Representative photomicrographs of MEG-3 and PGL-3 co-condensates imaged *in vivo* in 2 or 4-cell embryos or assembled *in vitro*. Scale bars are 1 μm. Representative *in vivo* images were selected from 8 embryos. Representative *in vitro* condensates were selected from data quantified in b and c. Additional examples of MEG-3/PGL-3 condensates assembled in vivo are shown in Supplementary Fig. 5. Source Data for panels b, c and d are available in Supplementary Data Set 1.

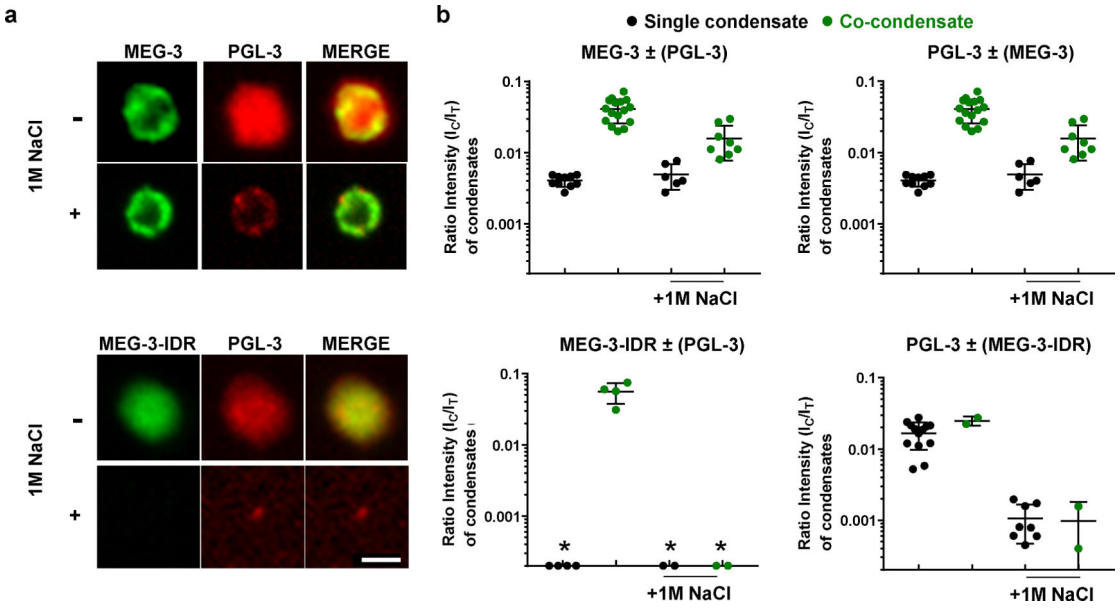

Fig. 5 –. MEG-3 forms a stable scaffold around the PGL-3 liquid phase

a. Representative images of PGL-3 (red), MEG-3 (green) or MEG-3-IDR (green) co-assemblies incubated in condensation buffer or buffer with 1M NaCl. Scale bars are 2 μm. Images are representative of data quantified in b.

b. Graphs showing the relative proportion of PGL-3 (right panels), MEG-3 (top left panels), or MEG-3-IDR (bottom left panels) in condensates [calculated as the ratio of fluorescence in condensates (I_C) over total fluorescence (I_T)]. The y-axis is on a log scale. Single condensates are in black and co-condensates are in green. Each data point represents the average from 4 images collected in one experiment. For data points indicated by "*", no condensates were detected. Bars represent the mean ± SD. Source data for panel b are available in Supplementary Data Set 1.

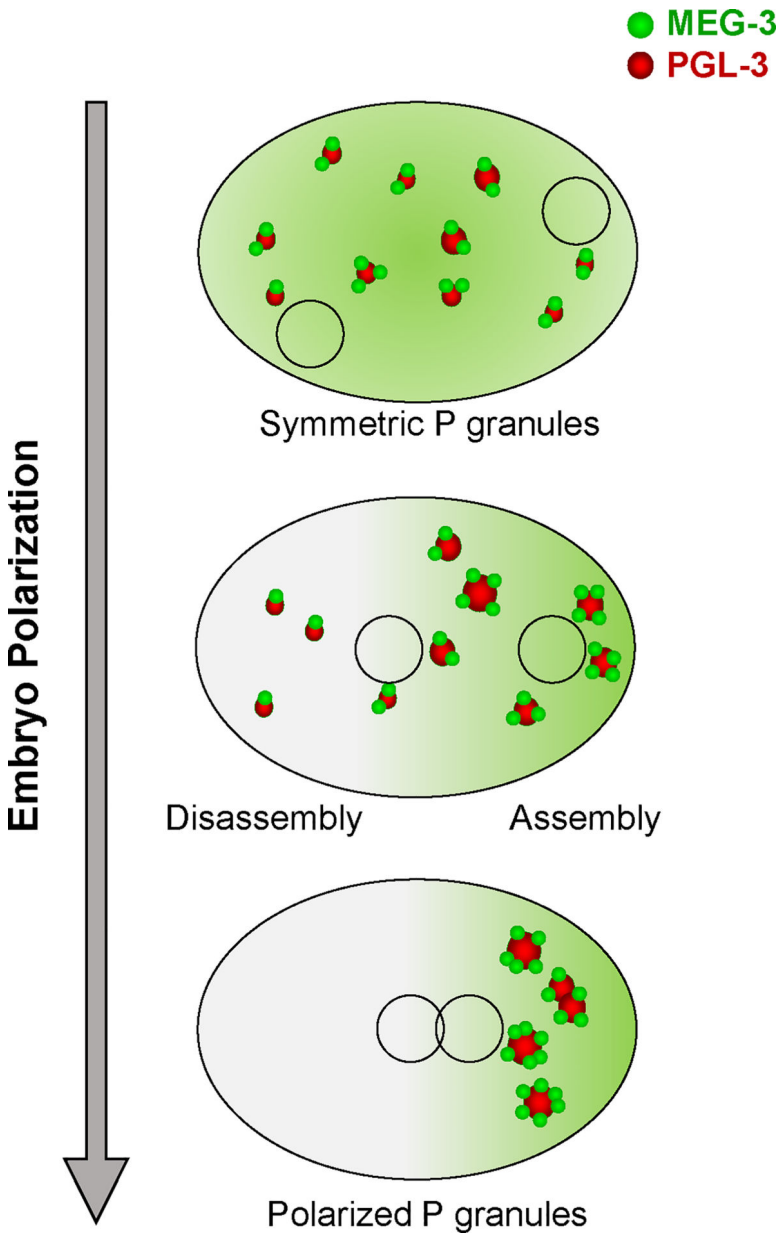

Fig. 6 –. Model for regulation of P granule assembly by the MEG-3 gel condensates.

MEG-3 condensates associate dynamically with PGL-3 condensates. Polarization of the embryo enriches MEG-3 in the posterior cytoplasm[18]. Preferential stabilization of PGL-3 condensates in the posterior creates an anterior-to-posterior flux of PGL-3 which destabilizes PGL-3 condensates in the anterior.

Table 1:

P granule protein dynamics in FRAP, temperature shift and extrusion assays

P granule protein	Fluorescence Recovery After Photobleaching (FRAP)		Temperature Shift (20°C→34°C)	Extrusion assay
	Recovery Rate	$t_{1/2}$ (calculated from recovery rate)		
MEG-3::GFP	0.0070 ± 0.0007 / sec	128.3 ± 16.4 sec	Stable	Stable
MEG-3::mCherry	0.0031 ± 0.0014 / sec	384.3 ± 198.8 sec	Stable	Stable
PGL-1::GFP	0.042 ± 0.004 / sec	20.73 ± 2.0 sec	Dissolves	Dissolves
PGL-3::mCherry	0.046 ± 0.008 / sec	21.9 ± 5.7 sec	Dissolves	Dissolves
GLH-1::GFP	0.028 ± 0.004 / sec	30.1 ± 5.2 sec	Dissolves	Dissolves
LAF-1::GFP	0.53 ± 0.08 / sec	1.5 ± 0.2 sec	Stable	Dissolves
DEPS-1::GFP *	<0.0001 / sec	NA	Partially Dissolves *	Partially Dissolves *

This table summarizes results presented in Figs. 1–3, and Supplementary Figs. 1–3. FRAP values are reported as the mean ± SEM. See related figures for n values.

* DEPS-1::GFP localizes to two types of condensates: a few, small, bright condensates present throughout the cytoplasm, and many larger, dimmer and posteriorly-localized condensates that correspond to P granules (Spike et al., 2008). Both are reduced in intensity after temperature shift (Supplementary Fig. 3). After extrusion, only smaller, bright DEPS-1 condensates are visible (Supplementary Fig. 3).